Progress in Additive Manufacturing (2025) 10:6279–6293
https://doi.org/10.1007/s40964-025-00969-x

RESEARCH

Mechanical behavior, microstructural evolution and texture analysis of AA2024-T351 processed by multi-layer friction surfacing with high build rates

Marius Hoffmann[1] · Arne Roos[1] · Benjamin Klusemann[1,2]

Received: 15 November 2024 / Accepted: 9 January 2025 / Published online: 29 January 2025

Abstract
Solid-state additive manufacturing (AM) processes such as multi-layer friction surfacing (MLFS) can overcome typical disadvantages of fusion-based AM such as high residual stresses, porosity or hot cracking. The tool-less process setup of MLFS prevents contamination of the resulting components, e.g., caused by wear or the use of lubricants. The present study investigates MLFS for the precipitation-hardenable alloy AA2024-T3 using a process parameter that yields a high build rate relevant for industrial applications. The fatigue performance is shown and the microstructural and the mechanical anisotropy is examined. The fatigue properties in deposition direction show a high cycle fatigue limit of 170.5 MPa and a decrease in the maximum stress level compared to the base material due to precipitate overageing. The microstructure shows a Brass$\{011\}\langle 211\rangle$ texture at the bottom of the layers due to the application of high axial forces. In the center of the layer, no preferred texture was observed, while B$\{\bar{1}12\}\langle 110\rangle$/$\bar{\text{B}}\{1\bar{1}\bar{2}\}\langle\bar{1}\bar{1}0\rangle$ shear textures were observed at the top part of the deposited layers. An elongated grain morphology with aspect ratios above 2 is present over the entire layer height. These microstructural characteristics cause anisotropy in mechanical properties, with highest ultimate tensile strength and elongation in deposition direction, i.e., 408 ± 5 MPa and 18 ± 3 % respectively, and the lowest values along the build direction, i.e., 377 ± 21 MPa and 9 ± 3 % respectively. The observed behavior is of considerable importance for the industrial design and application of components manufactured with MLFS as they show that MLFS can also result in anisotropic material properties, depending on the chosen process parameters. It requires careful selection of the right combination of stud material and process parameters to achieve isotropic properties in the deposited structure.

Keywords Multi-layer friction surfacing · AA2024 · Anisotropy · Mechanical property · Fatigue

1 Introduction

In recent years, solid-state processes have been increasingly studied for their suitability as additive manufacturing (AM) technologies, which is reflected in the growing number of publications [1]. Due to their solid-state nature, no material melting occurs, which overcomes various disadvantages of fusion-based AM processes, such as high residual stresses, inhomogeneous microstructures, porosity or hot cracking [2, 3]. For example, porosity and thermal residual stresses or epitaxial solidification resulting in columnar grains along the build direction, leading to anisotropic material properties, e.g., in powder based AM processes using aluminum alloys [4, 5]. Interlayer or post-processing has shown to improve the properties of AM structures. For example, interlayer hot rolling leads to a reduction in porosity and an increase in dislocation density, which results in grain refinement through recrystallization and an improvement in mechanical properties due to dislocation strengthening in direct energy deposition [6]. In addition, friction stir processing as interlayer post-processing reduces the anisotropy in direct energy deposition builds by eliminating large pores and refining grains [7]. Some of the recently investigated solid-state AM processes are either tool based such as friction

✉ Marius Hoffmann
marius.hoffmann@hereon.de

Arne Roos
arne.roos@hereon.de

Benjamin Klusemann
benjamin.klusemann@hereon.de

[1] Helmholtz-Zentrum Hereon, Geesthacht, Germany

[2] Leuphana University Lüneburg, Lüneburg, Germany

stir AM [8], friction screw extrusion AM [9], SolidStir AM [10] and additive friction stir deposition (AFSD) [11] or the tool-free friction surfacing (FS) process in its multi-layer variant, i.e., multi-layer friction surfacing (MLFS) [12]. In particular, AFSD and MLFS builds have shown no anisotropic mechanical properties in terms of strength properties [13, 14]. Besides its advantages, AFSD comes with the disadvantage of the necessity of a tool, which often requires a lubricant to reduce friction between tool and feed material. Phillips et al. [15] for example showed that the often used graphite tool lubricant leads to contamination at the layer interfaces, resulting in anisotropic material properties. Also Feng et al. [16] and Qiao et al. [17] observed anisotropy regarding tensile strength in AFSD, i.e., a lower strength along the build direction due to a weaker interlayer bonding, using AA2024 and AA6061, respectively. Shen et al. [18] observed different tensile strength in AA5B70 single-layer AFSD with higher tensile strength along the transversal direction compared to the deposition direction. Besides the contamination with lubricants, the layer interfaces can be significantly weakened by oxide layers. For example, in friction stir welding, insufficient stirring results in the formation of kissing bonds [19], which prevents the formation of a metallurgical bonding. By lowering the weld pitch, i.e., the distance traveled by the tool per revolution, oxides get dispersed more finely and therefore do not have an adverse effect on mechanical properties [20]. Also in solid-state AM processes such as AFSD or FS, the formation of oxide layers on top of FS aluminum layers is unavoidable [12, 21]. They remain in the interface when the stirring during the process is insufficient as observed in AFSD by Phillips et al. [22]. Otherwise, they can be disrupted by plastic deformation and friction [23]. Due to the tool-less nature of MLFS, the use of and the contamination with lubricants are not an issue and a sufficient stirring during the process will disperse the existing oxide layer [23].

In FS, the tip of a rotating consumable stud material is pressed onto a substrate material, resulting in heat generation due to friction. This leads to plastic deformation of the stud tip, generating additional heat during the process. By superimposing a relative translational movement between stud and substrate material, material is sheared off from the stud tip and deposited onto the substrate. Due to the relative simple process setup and the solid-state nature, FS offers a wide range of feasible material combinations such as steel [24, 25], titanium [26, 27], aluminum [28] and dissimilar material combinations like aluminum on steel [29, 30].

High-strength Al alloys, such as the Al–Cu–Mg alloy AA2024, are often used in the aerospace industry. To be able to employ the FS process, the deposited material has to fulfill the requirements of the industry regarding mechanical properties. As shown in FS studies of precipitation-hardenable aluminum alloys, the thermal history alters the mechanical properties due to overageing of strengthening precipitates [31, 32]. By adaption of the FS process parameters, the process temperature, its influence on the microstructure, i.e., on grain size [33], texture [34] and precipitates, and thus the mechanical properties [35] can be tailored. In order to fulfill the requirements of AM processes, high productivity, i.e., high deposition rates, is essential in addition to the desired mechanical properties. The focus of the present study is to investigate microstructure and mechanical properties in MLFS using a process parameter that leads to a high material deposition rate by applying a compromise parameter for thick and wide layers with a high stud travel speed. The deposition rate is one of the variables that can be adjusted for the FS process in order to achieve high deposition efficiency, which is lower in FS compared to other solid-state AM processes due to the flash formation, reducing its economic efficiency. A high deposition rate can therefore counteract this problem. In addition, the mechanical properties of the precipitation-hardenable aluminum alloy AA2024 were only investigated in a single direction in the previous studies. However, especially for the industrial application of the MLFS process, the knowledge of the directional dependency of AA2024 at a high production efficiency is inevitable, which is why this knowledge is a necessary prerequisite for the application of MLFS. This study fills this knowledge gap. Additionally, the present study is the first to present information on the fatigue behavior of as-deposited MLFS for precipitation-hardenable AA2024.

2 Materials and methods

2.1 Materials and FS process

In order to deposit MLFS stacks, AA2024-T351 was selected as the stud material with the stud dimensions of 20 mm (diameter) x 125 mm (length). Two 4 mm and one 25 mm thick AA2024-T3 sheets (300 mm long and 150 mm wide) were used as substrates to investigate mechanical and microstructural properties of the deposited MLFS material and in the layer-substrate interface. Table 1 gives an overview of the three MLFS stacks built, the substrates used and the characterizations carried out. A 12 mm thick AA7050 plate was utilized as backing to enhance heat transfer from the process zone.

For all deposits within the three MLFS stacks, identical parameters of 19 kN, 650 rpm and 10 mm/s were applied as axial process force, rotational spindle speed and translational speed, respectively. All MLFS stacks were built in force-controlled mode. The FS process parameters were selected based on a study, where the influence of the parameters on the deposition rates and on the mechanical properties has been investigated in detail for AA2024 [35]. The parameter

Table 1 Overview of the MLFS stacks built, the substrates used and the characterizations carried out

MLFS stack	Substrate thickness [mm]	Characterizations
MLFS-1	4	Fatigue and tensile test of MLFS stack material, hardness
MLFS-2	25	Tensile test of layer-substrate interface, hardness, microstructure
MLFS-3	4	Fatigue and tensile test of MLFS stack material

selected is a compromise between thick and wide layers, a high travel speed and a high MLFS mechanical strength. The goal is to achieve high material deposition rates and high strengths at the same time. Before starting the deposition of each subsequent layer, a new stud was employed while the whole setup cooled down to room temperature to allow the same initial conditions for the deposition of each layer. Within the manufacturing of each MLFS stack, no post-processing of layers was performed. To perform the FS processes, a specially designed FS machine (Henry Loitz Robotik, Germany) was used. It allows processes in a working area of 1.5×0.5 m^2 while applying process forces up to 60 kN, rotational speeds up to 6000 rpm and a maximum torque of 200 Nm. During the process, the machine acquires process data, i.e., axial force, displacements in all working directions, rotational speed and spindle torque.

The deposited MLFS stacks were examined through microstructural investigations, mechanical tests (fatigue test, tensile test and hardness test) and residual stress measurement as described in the following:

2.2 Sample preparation

For the hardness testing as well as for the microstructural analyses of the MLFS stacks, specimens were cut using an Axitom cutting machine and metallographically prepared using a Tegramin-20 grinding and polishing machine (both Struers, Denmark). During sample preparation, the specimens were ground using P320 grit size grinding paper, followed by fine grinding using 9 µm diamond suspension for two minutes each. They were polished afterward using 1 µm diamond suspension for four minutes. Samples prepared for electron-backscatter diffraction (EBSD) investigation were vibration polished using colloidal silica suspension (0.04 µm) for additional two hours. Etching of the samples was performed using Dix–Keller reagent (95 % distilled water, 3 % HNO_3, 2 % HCl, 1 % HF) for 10 s.

2.3 Microstructure

The Quanta 650 FEG scanning electron microscope (SEM) (Thermo Fisher Scientific Inc., USA) with an EDAX Velocity series EBSD detector (AMETEK Inc., USA) was used to examine the microstructure. The scans were performed across the layer-substrate interface to the top of the first layer in the center of MLFS-2. A step size of 0.2 µm, a working distance between 15 and 17 mm and a voltage of 15 kV were selected as EBSD scan parameters. The EBSD data were analyzed using MTEX toolbox version 5.8.1 in MATLAB (The Mathworks Inc., USA), selecting a misorientation threshold of 2° to define grain boundaries, i.e. low-angle grain boundaries (LAGB), as well as a minimal grain size of 3 pixels. Grain boundary misorientations greater than 15° are referred to as high-angle grain boundaries (HAGB).

The geometrical analysis, i.e., measurement of average layer width and thickness, was performed with a VHX-6000 digital microscope (Keyence, Germany).

2.4 Mechanical tests

ASTM E8 - Type 3 tensile specimens as well as EN 6072 Mini T-Type fatigue specimens were extracted from the three MLFS stacks. Their geometries are given in Fig. 1d, e. Tensile tests were intended to determine the mechanical properties of the MLFS stacks and its directional dependency. Therefore, the specimens were extracted in different orientations, i.e., parallel to the build direction (0°), parallel to the deposition direction (90°) as well as diagonal in a 45° orientation. Furthermore, the mechanical layer–substrate interface properties were tested with tensile specimens obtained from MLFS-2 parallel to the build direction. The extraction position was chosen that the upper half consisted of MLFS material and the lower half of substrate material. An overview of all extracted specimens is given in Fig. 1a–c. The tensile tests were conducted displacement-controlled (0.5 mm/min) using an universal tensile machine with a 5 kN load cell (ZwickRoell, Germany). The displacement during tensile tests was recorded by a laser extensometer (Fiedler Optoelektronik GmbH, Germany).

The fatigue tests were carried out using a 10 kN load cell servo-hydraulic testing machine (Schenck, Germany), applying a stress ratio of R=0.1 in a sinusoidal waveform with a constant force-controlled amplitude at a frequency of 10 Hz. Four specimens were tested at each load level. Testing was stopped when the specimens reached the predefined fatigue limit of 10^7 cycles. The specimens reaching 10^7 cycles were non-destructively tested for cracks using Y.Cougar µCT system (YXLON International GmbH, Germany), which enables crack analysis with a minimum voxel

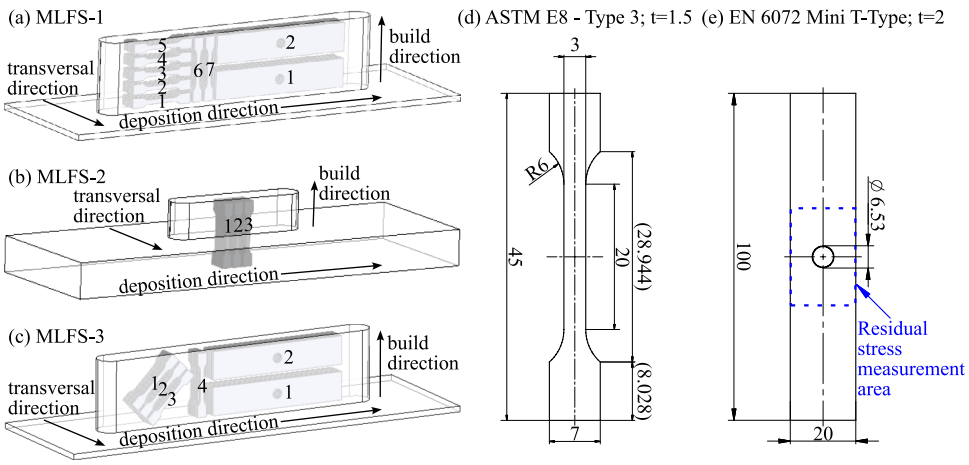

Fig. 1 Positions of all tensile and fatigue specimens extracted from the three MLFS stacks (**a**)–(**c**). ASTM E8 - Type 3 tensile specimen (**d**) and EN 6072 Mini T-Type fatigue specimen geometries (**e**). All dimensions are in mm

size of 40 x 40 x 40 µm^3. If no cracks could be detected, they were re-tested at a significantly higher load level.

Hardness tests in accordance with DIN EN ISO 6507 were performed using a Durascan 70 G5 automated hardness testing machine (EMCO-TEST Prüfmaschinen GmbH, Austria). For each indentation, a load of 0.2 kg using a Vickers indenter (136° opening angle) was applied. Hardness line measurements from the bottom of the substrate to the top of the stacks MLFS-1 and MLFS-2 with a distance between the indentations of 0.15 mm along MLFS stack build direction were recorded.

All mechanical tests (tensile, fatigue and hardness tests) were carried out six months after the deposition process. During this time, the specimens were stored at room temperature (~20°C), i.e., post-process natural aging occurred.

2.5 Residual stress measurement

Residual stress measurements were performed on two fatigue specimens using high-energy X-ray diffraction (XRD) at the P07B beamline in the synchrotron source PETRA III at Deutsches Elektronen Synchroton (DESY) in Hamburg, Germany, before the fatigue test. The beamline has a photon energy 87.1 keV and the beam has a size of 0.1 x 0.1 mm^2. In each specimen, a total area of 20 x 30 mm^2, see Fig. 1 (e), with a step size of 0.5 mm was scanned, resulting in a total of 2.501 scans/specimen. Debye–Scherrer diffraction rings were detected in transmission through the specimens by a two-dimensional Perkin Elmer XRD 1621 detector with a pixel size of 200 x 200 µm^2 and an active area of 2.048 x 2.048 pixels. From the diffraction pattern, the Al{311} peak position was analyzed to obtain the scattering angle 2θ. An azimuthal integration in four sectors, i.e., 0°, 90°, 180°, 270°, in a range of ± 10° was performed using the software FIT2D [36]. The sectors 0° and 180° were averaged to obtain the 2θ scattering angles in horizontal direction, while the average of 90° and 270° delivers the average 2θ angle in vertical direction. A stress free sample was measured as a reference in order to obtain the stress free scattering angle θ_0.

3 Results and discussion

Figure 2 shows the stacks MLFS-1 and MLFS-2 as well as the cross sections of the stacks MLFS-2 and MLFS-3. The MLFS stacks have an overall average layer thickness of 1.12 ± 0.12 mm, a layer width of 22.24 ± 0.48 mm and a bonded width of 16.80 ± 2.14 mm. This results in an average deposition rate of 41.55 g/min.

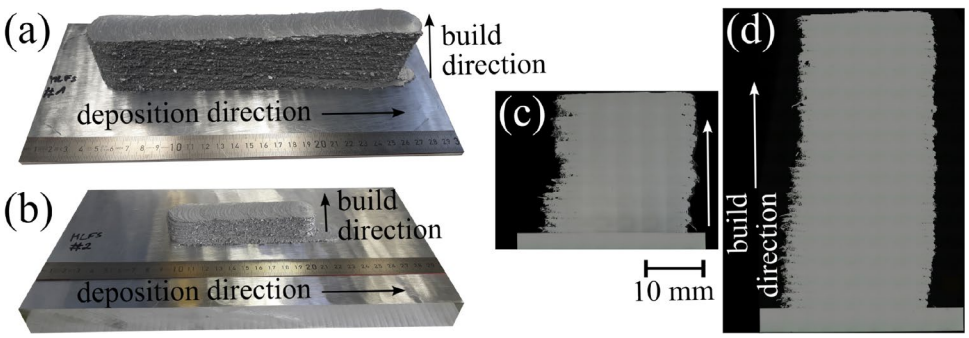

Fig. 2 MLFS stacks MLFS-1 (**a**), and MLFS-2 (**b**) as well as cross sections of MLFS-2 (**c**) and MLFS-3 (**d**)

3.1 Microstructure

An EBSD scan was performed starting in the substrate toward the top of the first layer of MLFS-2 in order to evaluate the changes of the microstructure in the layer–substrate interface as well as over a whole deposited FS layer. The corresponding inverse pole figure (IPF) map is given in Fig. 3. The substrate material shows comparably large grains. At the interface, there is a discontinuity in grain size as the layer materials exhibit a fine, recrystallized microstructure. In order to be able to have a deeper analysis of the microstructure in the layer, the scan on this side was divided into 100 µm sections. Average grain sizes, grain morphology, i.e., aspect ratio, the ratio of HAGB-length to LAGB-length as well as textures were analyzed in these sections, which is discussed in the following.

The grain size analysis, Fig. 4a, gives a trend already observed in literature [37], where, due to variation in strain and cooling rate across each layer, the grain sizes at the bottom (1.63 ± 0.68 µm) and the top (1.70 ± 0.77 µm) of each layer are slightly smaller compared to the center (1.75 ± 0.80 µm). This effect can also be seen here, but is less pronounced. The aspect ratio of the grains is given in Fig. 4b. Often, equiaxed grains are reported for the microstructure of FS layers as a result of the recrystallization process [34]. In the present study, however, slightly elongated grains with an aspect ratio of about 2 in transversal direction are present, which might be a result of the high axial force applied during the deposition process.

Furthermore, the ratio of HAGB/LAGB was analyzed, Fig. 4c. The results show that the ratio is the highest in the center and decreases toward the top and the bottom of the layer. In the investigation of Kallien et al. [37], the ratio of HAGB/LAGB showed the opposite trend, i.e., it increased close to the interfaces in the bottom and top part of the AA2024 and AA5083 layers. The main difference between

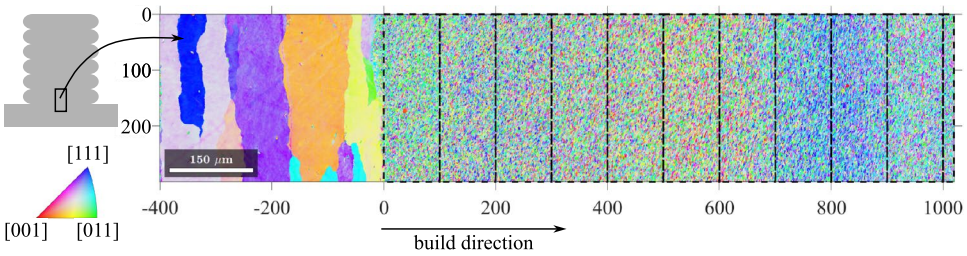

Fig. 3 IPF-Map of the top part of the substrate (negative position) as well as the first layer of MLFS-2 (positive position) scanned in the center of the MLFS stack as indicated by the schematic cross section in the top left corner. The layer is divided in 100 µm segments for detailed microstructural analysis. The segments are indicated by the black dashed rectangles

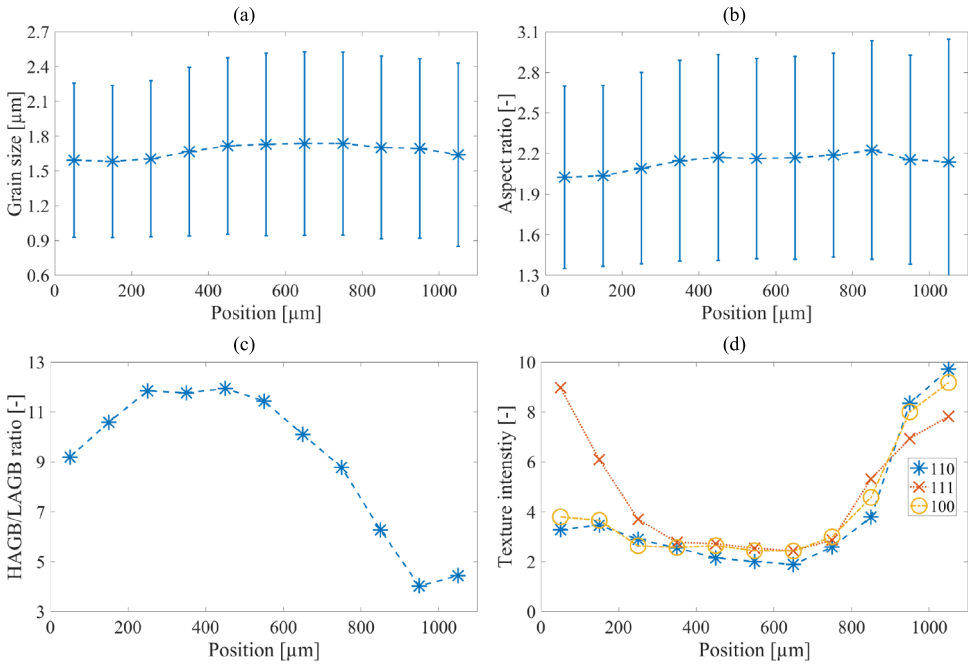

Fig. 4 Analysis of the average grain size (**a**), the average aspect ratio (**b**), the HAGB/LAGB ratio (**c**) and the texture intensities (**d**). The values are calculated from the MLFS-2 EBSD data in the segments indicated in Fig. 3

these two studies is the process parameters selected, where in the present study, significantly higher axial forces and travel speeds as well as slightly lower rotational speeds were selected that lead to the formation of a distinct texture in bottom and top of the layer and a random texture in the layer's center. Typical for regions with a strong texture, the amount of LAGB increases and therefore the ratio of HAGB/LAGB decreases [38]. The texture analysis reveals that along each layer height different textures are present, Fig. 4 (d), which is explored in detail via the pole figures and orientation distribution functions (ODF) in Fig. 5.

At the bottom, the deformation texture component Brass{011}⟨211⟩ is present in the first 200 µm of the layer, see Fig. 5a. This kind of texture is a common rolling texture in high stacking fault energy materials such as Al alloys [39]. Due to the characteristic of the FS process, the material at the bottom of the layer is deposited in front of the stud's rotation axis [40]. As soon as the rotational axis of the stud passes the positions where material is already deposited on the substrate, this material is subjected to compressive forces. These can lead to further plastic deformation, known as rolling deformation [41], which results in a corresponding texture. The relative high axial force selected in this study

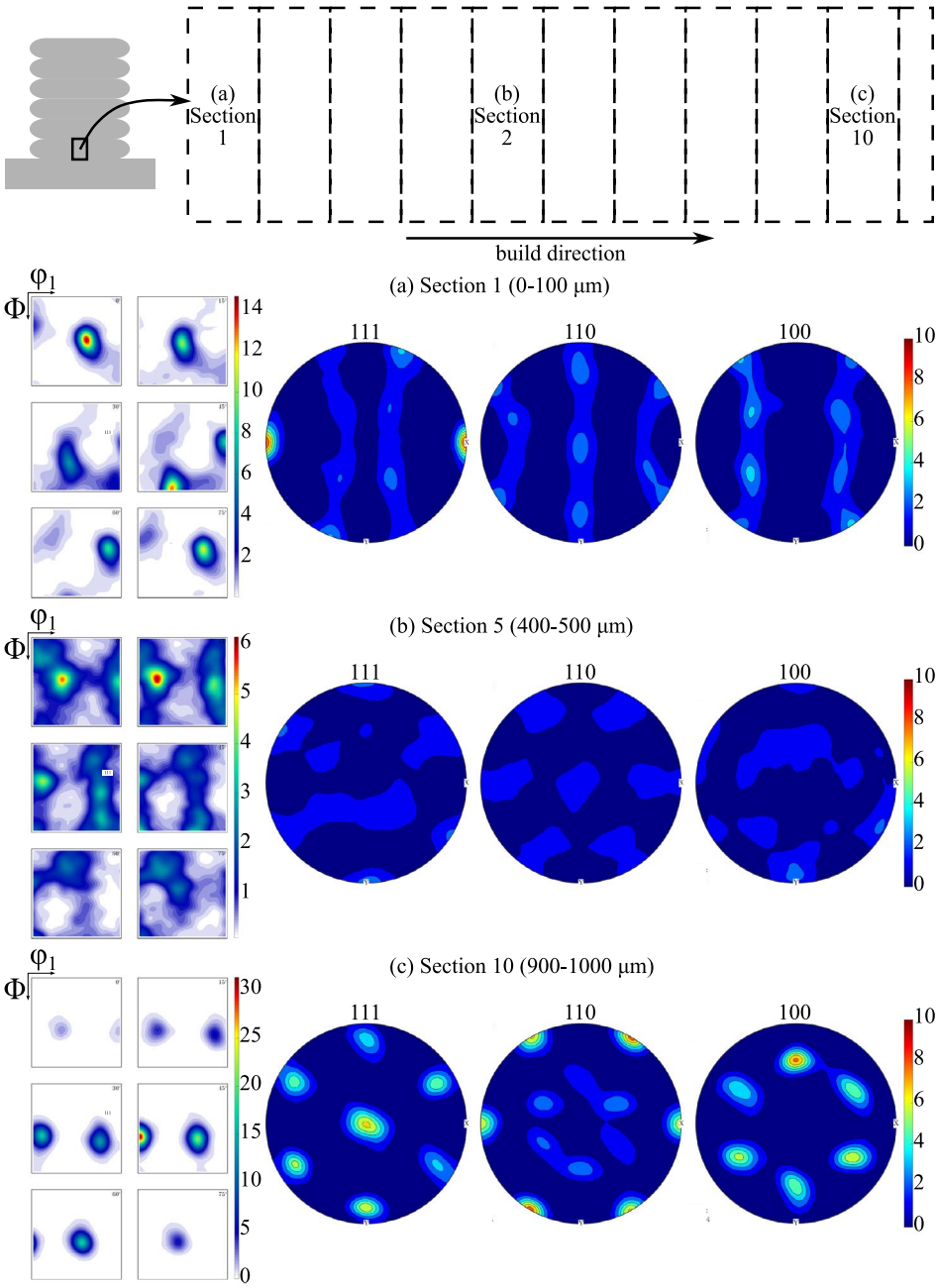

Fig. 5 ODF plots and pole figures of Section 1 (0–100 µm) (**a**), Section 5 (400–500 µm) (**b**) and Section 10 (900–1000 µm) (**c**) of the IPF maps in Fig. 3

contributed to an increased plastic deformation of the material in the bottom of the layer. In the center of the layer, Fig. 5b, no clear texture components can be identified, thus the texture can be considered as random. The formation of a simple shear texture was identified in the area of about 300–400 µm close to the top of the layer with an increasing intensity toward the top. In this part of the layer, the texture is defined by the components $B\{\bar{1}12\}\langle 110\rangle$ as well as $\bar{B}\{1\bar{1}\bar{2}\}\langle\bar{1}\bar{1}0\rangle$, Fig. 5 (c). In a study by Hoffmann et al. [40], this texture was correlated to the material flow during the FS process, where the top part of the layer forms at the rear edge of the stud. At this position, the stud material only shears off from the stud tip and is not exposed to high temperatures or plastic deformations anymore, which does not lead to further recrystallization or texture changes.

3.2 Mechanical testing

3.2.1 Hardness

The hardness line measurements in MLFS-1 and MLFS-2 are shown in Fig. 6. As already reported in literature [35, 37], the periodical hardness distribution coincides with the layers in the MLFS stacks. This means a lower hardness is present in the center of each layer, whereas close to the interfaces, higher hardness was measured. The average hardness is approximately 115 HV0.2, which is lower compared to the AA2024-T351 base material hardness due to overageing during the MLFS process [32]. Comparing both MLFS stacks clearly shows that a higher number of heat inputs in MLFS-1 does not result in a further hardness decrease, i.e., the microstructure can be considered as completely overaged. The top part of the MLFS stacks, i.e., the top 4–5 mm, experience less overageing due to the lower number of thermal cycles, i.e., a higher hardness of about 145 HV0.2 is determined.

As also reported by Ehrich et al. [42], a 7.5 mm deep HAZ consisting of three different zones based on different hardness changes can be noticed for MLFS-2 with a total depth of about 7.5 mm, see Fig. 6. In HAZ zone 1, the hardness decreases over 2 mm from around 150 HV0.2 toward 120 HV0.1 at the layer–substrate interface. In zone 2, which is about 3 mm deep, the hardness is more stable in the range between 146 and 150 HV0.2, whereas a lower hardness is detected in zone 3, which is about 135 HV0.2. Outside of the HAZ, the substrate hardness is about 152 HV0.2. Compared to MLFS-2, in MLFS-1, only one HAZ zone exists due to the significant lower substrate thickness, in which the hardness decreases toward the layer–substrate interface.

3.2.2 Tensile test

Compared to the local variations in mechanical properties determined during hardness testing, tensile tests provide a more general insight into the mechanical behavior aggregated over larger areas. The tests were conducted in three different orientations, i.e., along build direction (0°), along deposition direction (90°) and at a 45° angle, to determine the dependency of load direction on the mechanical properties. The comparison of the UTS and elongation (A_t) in the different orientations and positions shows that the specimens taken in the deposition direction (90°) have the highest average UTS (408.2 ± 4.9 MPa) and elongation values (17.7 ± 2.5 %) and show a ductile fracture behavior, Fig. 7. Figure 8 compares the data of the tensile test results. In terms of UTS, the range of values is the lowest in the deposition direction. The minimum, median and maximum UTS values are 384.2, 407.9 and 415.7 MPa, respectively. In the deposition direction, no relation between layer interfaces and fracture location is found, Fig. 9d. Furthermore, the variation of the extraction position along the build direction does

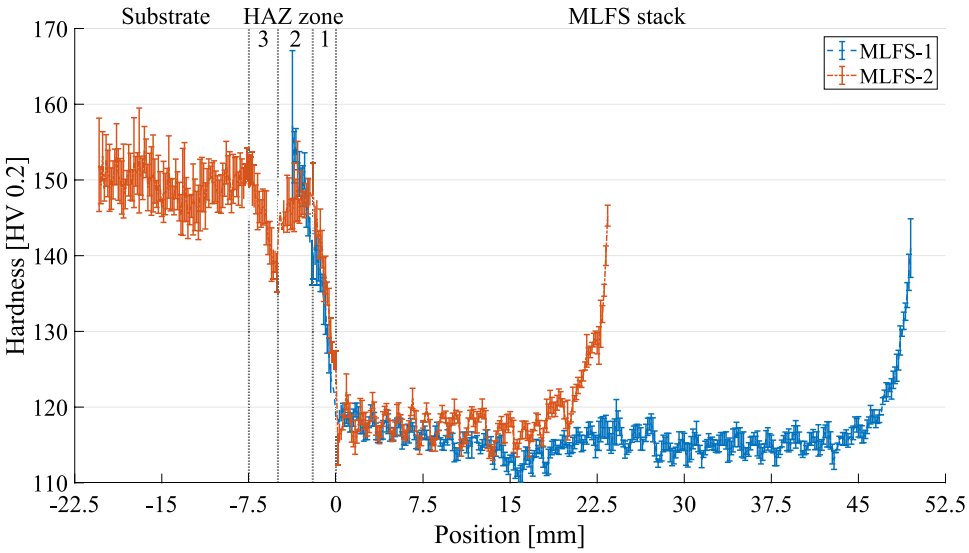

Fig. 6 Hardness measurements in MLFS-1 and MLFS-2 from the bottom of the substrate to the top of the MLFS stacks. The negative positions refer to the substrate, the positive positions to the MLFS stack material. The HAZ of the substrate is indicated by the dashed lines and is subdivided in three zones

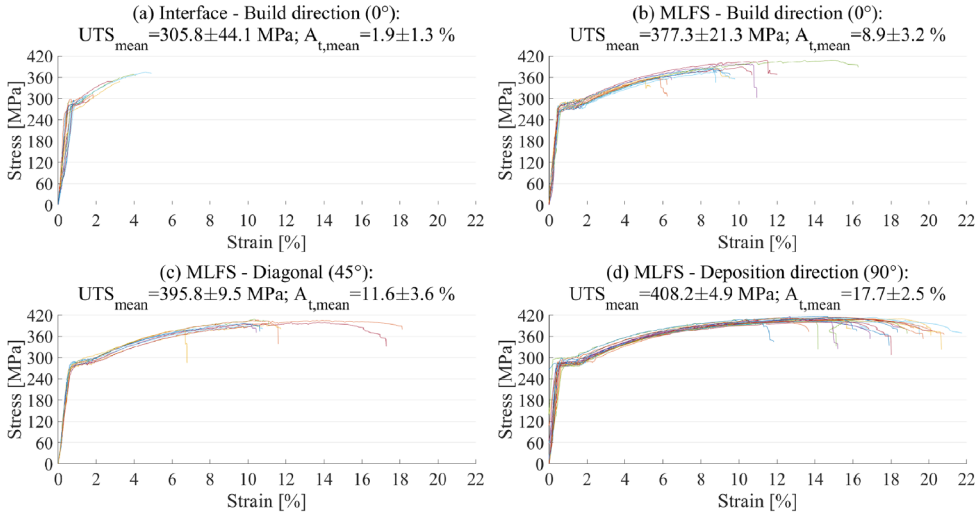

Fig. 7 Stress–strain curves of the tested tensile specimen extracted in different orientations and positions from the three MLFS stacks

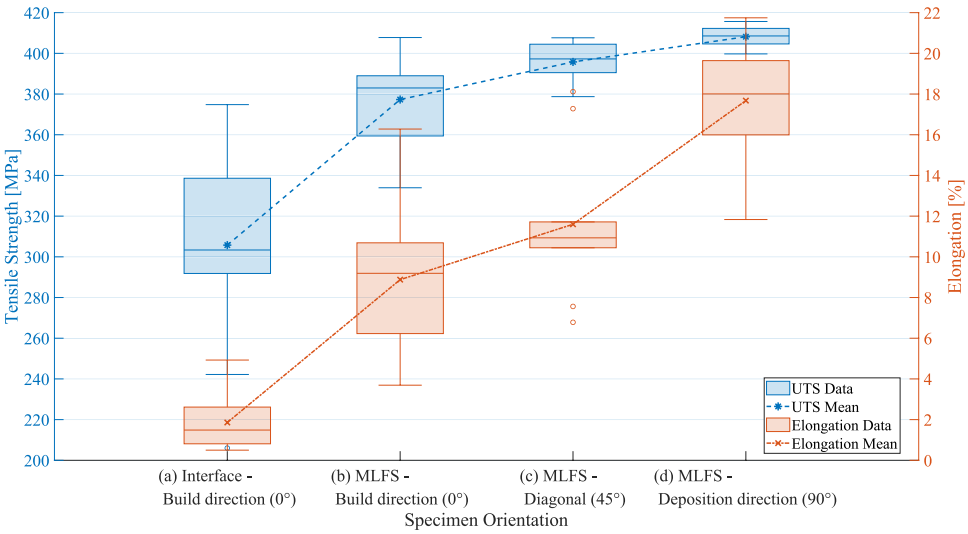

Fig. 8 Box plots of the four different specimen orientations regarding tensile strength and elongation

not lead to the trends observed in the hardness measurements, i.e., no higher strength was observed in the top of the MLFS stacks compared to the other regions. This is due to the offset of at least 2 mm of the tensile specimen extraction position from the very top of the MLFS stacks. Due to the geometry of the specimens, i.e., 7 mm specimen width and 3 mm gage width, which results in a 2 mm offset between the edge of the clamping area and the edge of the gage section, see Fig. 1d, the gage width of the specimens does mainly consist of overaged MLFS stack material. Therefore, possible higher strength values near the top cannot be noticed via the tensile tests. The fracture surfaces are shown in Fig. 10. The analysis confirms the ductile fracture behavior for the specimens extracted in the deposition direction, indicated by the dimples at the fracture surface, Fig. 10d.

A 45° angle between the specimen axis and the build direction results in reduced values for both UTS and elongation and an increased scatter of the measurement data compared to the specimens along the deposition direction. The minimum, median and maximum UTS values are 379.1, 396.8 and 407.6 MPa, respectively. The fracture surfaces are parallel to the interfaces, Fig. 9c, which might indicate that these interfaces withstand lower stresses in MLFS stacks.

The range of UTS values is the highest for the specimens along the build direction (0°). While the median and maximum values along the build direction in the MLFS stacks, i.e., 380.9 and 408.2 MPa, respectively, are nearly the same as for the deposition (90°) and diagonal (45°) direction, the minimum UTS significantly decreases to 330.1 MPa. Within the MLFS stacks, the lowest UTS and elongation values were observed along the build direction, i.e., 377.3 ± 21.3 MPa and 8.9 ± 3.2 %, respectively. The fracture surfaces of the MLFS specimens along the build direction are mainly parallel to the layer-layer interfaces, see Fig. 9b, which leads to the hypothesis of the layer interfaces as weak spots. The stress–strain curve analysis

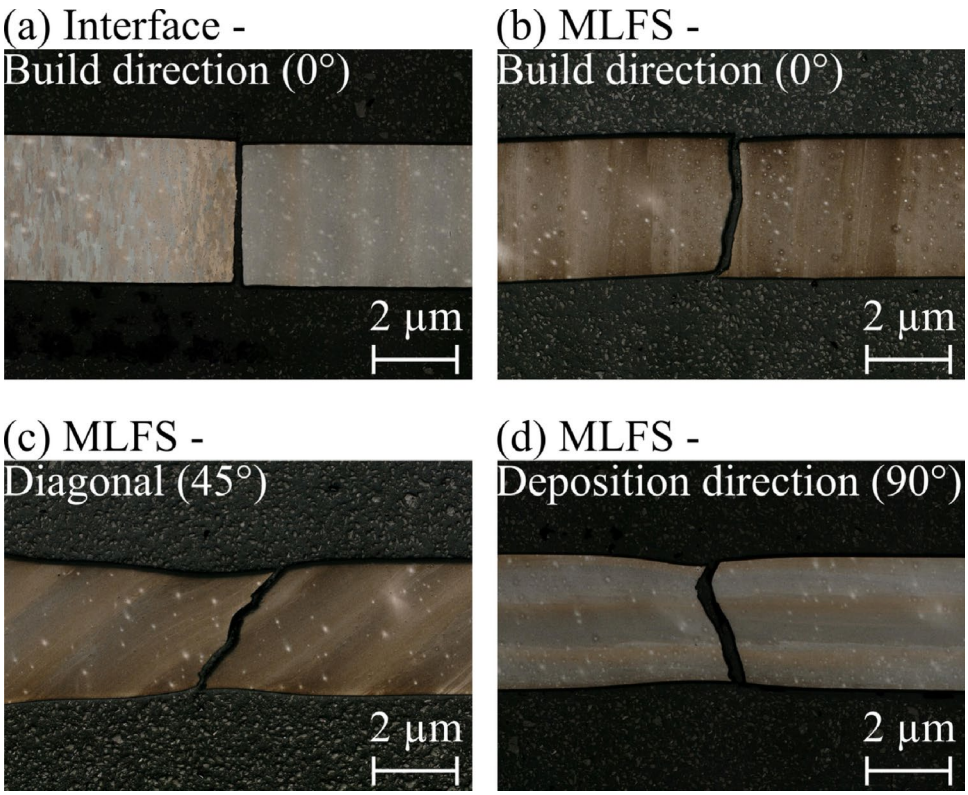

Fig. 9 Etched tensile specimen reveals fracture orientations parallel to the layer interfaces in build direction (0°) specimens over the layer–substrate interface (**a**) and in the MLFS stack (**b**) as well as in diagonal direction (45°) (**c**). For the specimens in deposition direction (90°), no preferred fracture orientation can be observed

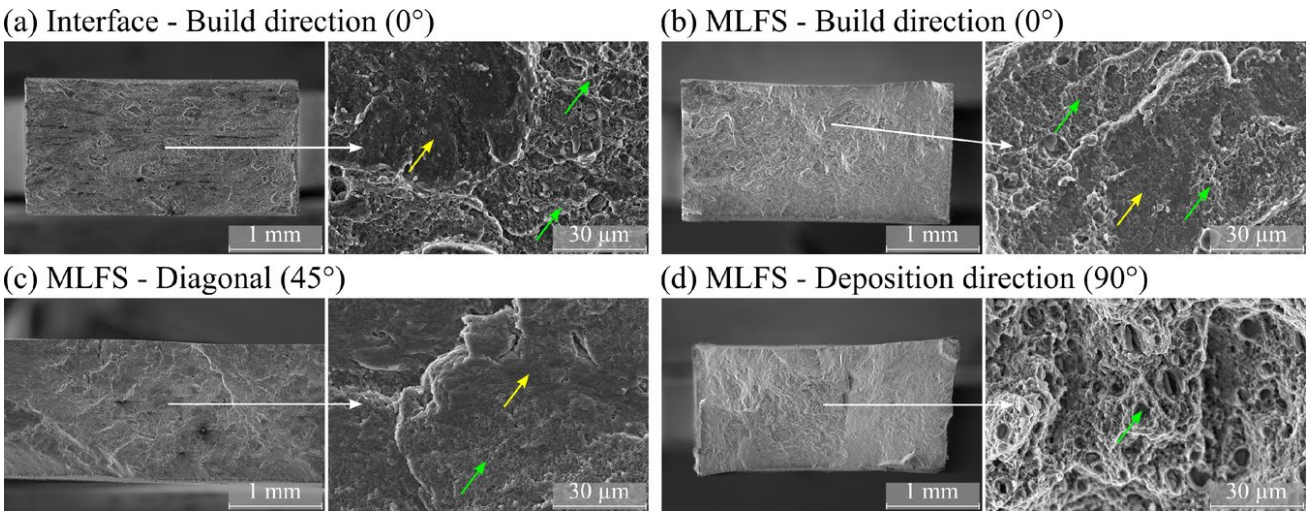

Fig. 10 The fracture surfaces of the tensile specimens in all orientations. The build direction (0°) (**a**, **b**) and the diagonal direction (45°) (**c**) specimens show a mixture of ductile fracture indicated by dimples (green arrows) and brittle fracture indicated by a lack of metallurgical bonding (yellow arrows). The fracture surface of the specimen in deposition direction (90°) only shows dimples (green arrows)

in Fig. 7b for the build direction specimens tested within the MLFS stacks leads to the assumption of a mixed ductile–brittle behavior. This is confirmed by the fracture surface analysis of the MLFS material specimens tested along build direction, Fig. 10b, which shows evidence of both ductile and brittle fracture. Areas of brittle fracture exhibit a smooth fracture surface.

The comparison of the build direction specimens extracted within the MLFS material and across the layer-substrate interface clearly shows that the layer–substrate

interface is weaker than the MLFS material and the layer–layer interfaces, indicated by the lower UTS and elongation values observed, i.e., 305.8 ± 44.1 MPa and 1.9 ± 1.3 %, respectively. All specimens tested along the build direction across the layer–substrate interface fractured at the layer–substrate interface, Fig. 9a. The specimens extracted in this orientation and position show the lowest UTS and elongation values overall. As all specimens fracture at the layer–substrate interface, the interface is the weak point in terms of mechanical load perpendicular to it. The build direction specimens tested in the layer–substrate interface indicate signs of a mixture of ductile and brittle fracture. Some tested specimens show plastic deformation of more than 4 %, while others break at comparably small elongations. The fracture surface confirms this for specimens fractured at the layer-substrate interface, which also shows a mixture of dimples and lack of metallurgical bonding, resulting in brittle fracture, Fig. 10a.

The results obtained for MLFS are similar to reported results in literature for similar solid-state AM process, such as friction stir additive manufacturing (FSAM) and AFSD [8, 16, 43]. For FSAM, tensile strengths between 292 and 392 MPa and elongations between 8.4 and 26.1 % in the weld direction were reported [43], while other researchers reached strengths between 275 and 490 MPa and elongations between 1 and 20 % [8]. For AFSD, higher strengths and elongations were observed, i.e., 473–532 MPa and 15.2−31.2 %, respectively [16]. Overall, the MLFS results lie between the results reported for FSAM and AFSD in terms of strength, while significantly higher strengths can be achieved using AFSD.

The observed behavior is of considerable importance for the design and application of components manufactured using MLFS. Particular attention should be paid to the load direction of the component to be manufactured, i.e., tensile loads normal to the layer–layer and layer–substrate interfaces should be avoided using the process parameters for high build rates investigated in this study. Alternatively, depending on the application, a different process parameter needs to be selected that results in a higher interface bond strength and ductility, but a lower build rate.

3.2.3 Causes of anisotropy

To determine the fracture location in relation to the position of the interfaces, a cross section of MLFS-2 has been analyzed in detail via SEM. The analysis reveals defects at the layer–substrate interface as shown in Fig. 11 that confirm the lack of metallurgical bonding. These defects reduce the bonded area at the layer-substrate interface and result in a stress concentration and multiaxiality at the interface (similar as for a notched tensile specimen). It is important to mention that such defects are discernible at the layer–substrate interface but not at layer–layer interfaces. Furthermore, at the layer–substrate interface, a drastic change of ductility exists due to the significant change in grain size as shown in Fig. 3. By applying the stress to the specimens across the layer–substrate interface, the finer grains in the layer material can plastically deform more than the ones of the substrate material. This results in additional shear stresses at the interface, which increase stress multiaxiality in this part of the specimen. In addition, the substrate material exhibits a higher hardness and a higher assumed strength than the layer material, which also leads to a different mechanical response of layer and substrate materials. These effects, i.e., stress concentration and multiaxiality as well as interface defects and different strengths, consequently lead to the lowest UTS and ductility values for the specimens tested at the layer–substrate interface.

No such effects were observed at the layer-layer interfaces. Therefore, different mechanisms seem to deteriorate the mechanical properties parallel to the build direction. As Rath et al. [14] and Sharifi et al. [44] did not observe anisotropic behavior for AA5083 MLFS stacks, the anisotropy might be related to the selected material in the present investigation, i.e., the precipitation-hardenable alloy AA2024, or the selected process parameters, that might lead to local differences of the material properties. However, as shown above, the selected process parameters result in the formation of two different textures in the MLFS stacks. A Brass$\{011\}\langle 211\rangle$ texture is formed in the bottom of the layers due to the high axial force. As the force was significantly lower in the AA5083 investigation by Rath et al. [14] and

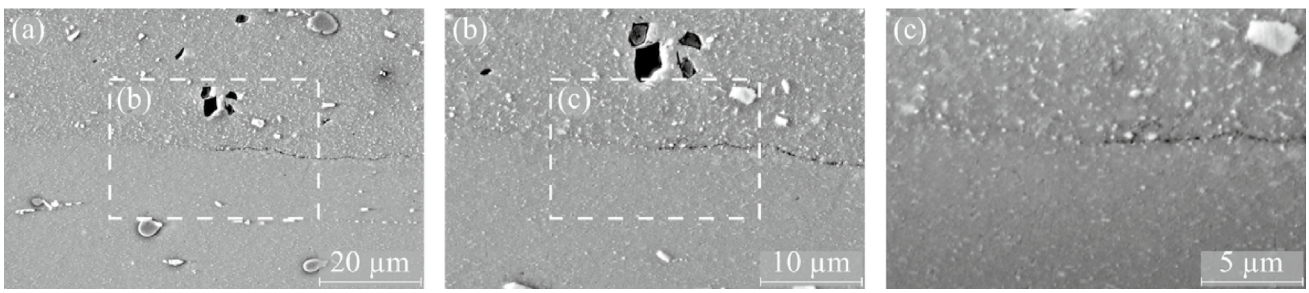

Fig. 11 Defects at the layer–substrate interface at 2.500x, 5.000x and 10.000x magnification of the cross section of MLFS-2

was not reported by Sharifi et al. [44], it can be assumed that no such texture exists in the AA5083 MLFS stacks described in the literature. As shown in an investigation of 2A12 aluminum alloy by Zhao et al. [45], Brass rolling texture enhances the UTS and slightly increases the elongation. Due to the local texture variations along layer height, i.e., rolling texture at the bottom of each layer and shear texture in the top part of the layer, dislocation movement is not uniform. In highly textured regions, the grains have similar orientations and therefore less energy for plastic deformation is required as low-angle grain boundaries provide lower resistance than high-angle grain boundaries to the dislocation movement. Therefore, regions that provide a texture will deform differently than regions with no preferential texture. As a result, all three regions have a different response to external load and deform differently. The MLFS stack material responds to the load like a composite structure in which the texture determines the fiber direction. Thus, it also provides anisotropic properties in different test directions. Especially at the layer–layer interface, a transition between shear and rolling texture might result in a discontinuity of the properties of the MLFS stacks leading to a delamination at the layer–layer interfaces.

Besides that, the microstructure analysis reveals an anisotropy in the grain morphology due to slighlty elongated grains in transversal direction. The strength increase by the grain size reduction σ_{GS} can be calculated using [46]

$$\sigma_{GS} = K \cdot d^{-1/2}, \tag{1}$$

where K is the Hall–Petch slope and d is the average grain size. An aspect ratio of 2 leads to a decrease of the grain boundary strengthening mechanisms by about 30 % and decreases even more for higher aspect ratios. Elongated grains cause anisotropy, which is also confirmed by the work of Cho et al. [47] where the grain shape affects the yield strength anisotropy by approximately 40 %. Therefore, it is assumed that the transition from shear texture (B$\{\bar{1}12\}\langle 110\rangle$ /$\bar{\text{B}}\{1\bar{1}\bar{2}\}\langle\bar{1}\bar{1}0\rangle$) to rolling texture (Brass$\{011\}\langle 211\rangle$) at the layer interfaces and the elongated grains mainly causes the anisotropy observed in the tensile test results of the MLFS stack material.

3.2.4 Fatigue test

The results of the fatigue tests, i.e., the Wöhler curves, are displayed in Fig. 12a and are compared to results from literature, i.e., fatigue test results for AA2024-T351 sheet material [48] as well as AA2024 friction stir welding (FSW) specimens [49]. The Wöhler curve of the specimens tested in the present study is located in between the two curves obtained from literature. Comparing to the FSW specimens, the MLFS specimens present higher maximum stresses. For both the MLFS and FSW specimens, a lower load needs to be applied to withstand same number of cycles as the sheet material. This might be related to the overageing of the microstructure occurring in FSW [50] and in MLFS specimens as discussed above. It is important to note that no direct comparison of the fatigue results is possible here as the present work uses a different specimen geometry compared to the others. The hole in the center of the specimen represents a geometric discontinuity that changes the stress distribution in the specimen compared to the ones in the other studies and leads to localized stress concentrations around the hole, significantly reducing the fatigue life. As the tensile tests reveal anisotropic material properties, the obtained fatigue results display the Wöhler curve for the strongest load direction. It can be expected that the maximum applied loads to withstand the same amount of cycles are reduced when the load is changed to 45°/diagonal orientation or 0°/build orientation. For the tested orientation, the high cycle fatigue limit is located at a maximum applied stress between 170.5 and 174 MPa. When the extraction positions, i.e., bottom and top of the MLFS stacks, are compared, a slightly higher cycle number can be observed for the specimens from the top, Fig. 12b. Since there is no significant difference in residual stresses for the two extraction positions, see Appendix A, and assuming that all fatigue specimens consist only of similar overaged microstructure, the differences between top and bottom could be due to process or test scattering. The high scatter in the fatigue tests must be taken into account accordingly in FS component design if maximum applied stress is above the MLFS high cycle fatigue limit of 170.5 MPa. The scatter of the data can have different causes, e.g., microstructural variations,

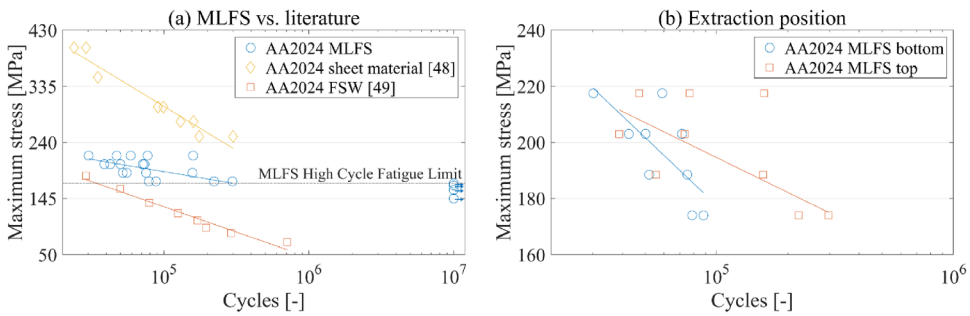

Fig. 12 Wöhler curve of the MLFS fatigue specimen in comparison to AA2024-T351 sheet material [48] and AA2024 FSW specimens [49] (**a**) as well as a comparison of the MLFS specimen extraction position (**b**)

i.e., grain size and texture, residual stress gradients, second phase particles or local imperfections. The fatigue specimens in the present study were extracted from two different positions along the build direction. At each height, five specimens were extracted along the transversal direction, i.e., from advancing to retreating side. As shown in several studies on friction surfacing using aluminum alloys, e.g., [40, 51], the microstructure is a result of the complex material flow during the friction surfacing process. For example, the advancing side often contains smaller grains compared to center and retreating side, whereas the top part of the layer presents shear textures. Similar results were reported for residual stresses [27], i.e., higher tensile residual stresses were observed on retreating side compared to the center and advancing side for Ti6Al4V single layers.

Figure 13 shows the fracture surfaces after fatigue tests of two different specimens, i.e., one that failed at a low cycle number at a high stress and one that failed at a high cycle number at a low stress. Both of them show fatigue typical fracture surfaces, i.e., a fatigue crack growth region, in which the crack growth can be detected by striation that formed during the cyclic loading of the specimen, and a fast fracture region, in which the final failure of the specimen occurred. The specimen that reached a higher cycle number at a lower load also shows a larger crack propagation region, which is a common observation in fatigue testing [52].

4 Conclusions

In the present study, AA2024 MLFS stacks with process parameters resulting in high layer thickness and width at high travel speeds were investigated regarding microstructure as well as tensile test anisotropy and fatigue performance. The findings are the following:

- High axial process forces lead to discontinuity of microstructure due to changes in texture across the layer–layer interface and to a decrease of HAGB/LAGB ratio in the interface region and thus to a change in mechanical properties.
- High axial process force results in the formation of a Brass$\{011\}\langle 211\rangle$ rolling texture in the lower 200 µm of the FS layers.
- Tensile tests show a directional dependency of UTS and elongation. Ductile fracture behavior with the highest UTS and elongation values is observed in the deposition direction. A mixture of ductile and brittle fracture behavior with lower UTS and elongation values is observed along the build direction.
- The anisotropy in the MLFS material is a result of the microstructure developed during the FS process, i.e., a transition from B$\{\bar{1}12\}\langle 110\rangle$/ $\bar{\text{B}}\{1\bar{1}\bar{2}\}\langle\bar{1}\bar{1}0\rangle$ shear textures in the top of the layers to Brass$\{011\}\langle 211\rangle$ rolling textures in the bottom of the layers and elongated grains. Over the entire layer height, elongated grains are observed in the transversal direction with an aspect ratio between 2 and 2.3. This leads to strength anisotropy due to decreased grain boundary strengthening mechanisms along the build direction.
- The mechanical properties of the specimens tested across the layer–substrate interface along the build direction exhibit the lowest UTS and elongation values. This is due to bonding defects and mechanical and microstructural discontinuities, i.e., a hardness and a grain size step respectively, at the interface, which lead to a local stress

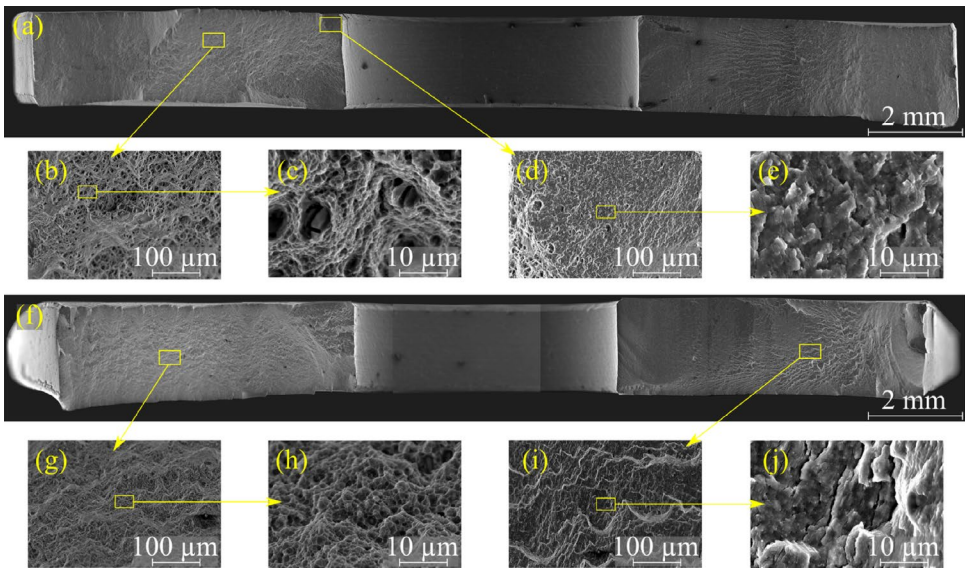

Fig. 13 Specimen that failed after around 30,200 cycles at 217.5 MPa (**a**) and specimen that failed after around 221,800 cycles at 174 MPa (**f**); both with enlarged areas showing a combination of fatigue crack growth region and fast fracture region presenting ductile fracture, indicated by striation (**d**, **e**, **i**, **j**) and by dimples (**b**, **c**, **g**, **h**) respectively

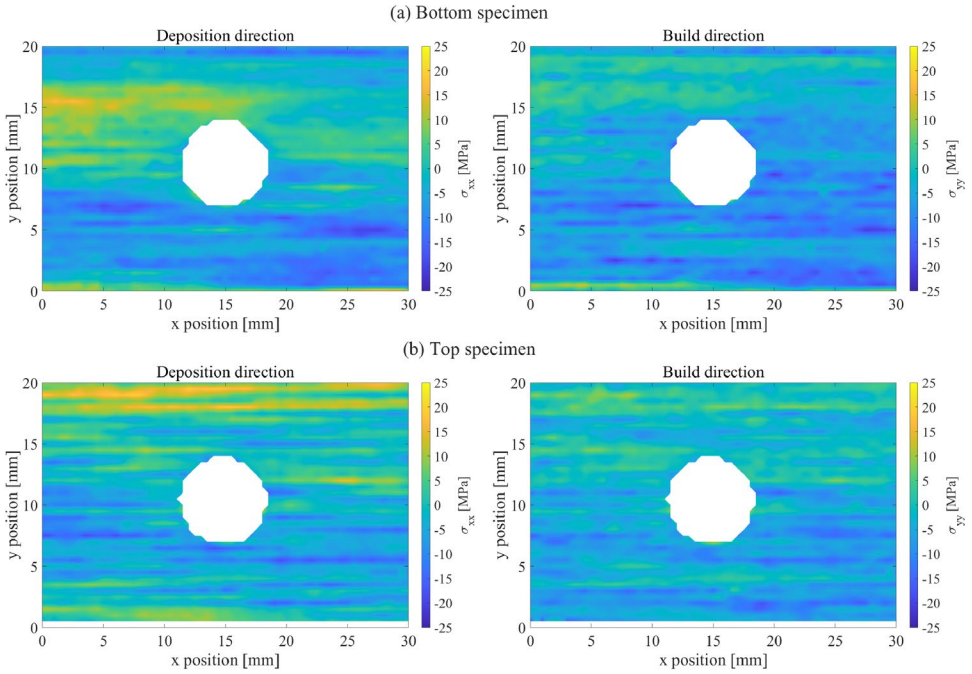

Fig. 14 Residual stress maps for specimens from the bottom (**a**) and from the top (**b**) of MLFS-1 in deposition and build direction

concentration and stress multiaxiality at the interface respectively.

- The MLFS fatigue specimens along the deposition direction must be tested with lower stresses due to the overaged microstructure to achieve the same number of cycles as the base material.

Appendix A: Residual stresses

The high-energy XRD residual stress analysis was performed using a specimen from the bottom and a specimen from the top of MLFS-1, see Fig. 1. The objective was to determine whether the residual stresses varied between the different specimen locations, potentially affecting the mechanical properties in the multi-layer deposits. The results for the residual stresses in deposition and build direction are shown in Fig. 14. The findings indicate that neither significant differences exist between the specimen extraction positions nor across the specimen heights and widths. The highest difference in residual stress in both specimens is approximately 40 MPa in the deposition and 35 MPa in build direction. The maximum tensile residual stresses in deposition direction are about 22 MPa (bottom specimen) and 20 MPa (top specimen). The maximum difference in residual stress in the build direction is slightly smaller (~35 MPa), with maximum tensile residual stresses of 15 MPa (bottom specimen) and 13 MPa (top specimen). Tensile residual stresses are more prevalent on the top side of the specimens, while compressive residual stresses appear to be more dominant on the bottom side. This situation might result in accelerated fatigue crack growth on the top side of the specimens. However, the magnitude of residual stresses is at ~7 % compared to typical AA2024-T351 yield strength values, which is around 280 MPa [53], which means that their influence could possibly be small and thus can be neglected regarding the fatigue performance. It is also worth noting that a periodic increase and decrease of residuals stresses can be identified in both specimens in Fig. 14, which might be correlated with the layers in the MLFS stacks. In each layer, there are variations in residual stresses from compressive to tensile that might result from the local temperature gradients during the FS process, which could weaken the bonding at the layer interfaces if tensile stresses exist in the interface region. A higher measurement resolution might be necessary to proof this as no correlation between tensile residual stress and the actual layer interfaces can be made.

Funding Open Access funding enabled and organized by Projekt DEAL. The work was carried out under the auspices of the AVAIL-DE project (project number 20W1906E), which is funded by the German Federal Ministry of Economic Affairs and Climate Action (BMWK) under the LuFo VI-1 program.

Data availability Data will be made available on request.

References

1. Elsevier: Scopus - Analyze search results - TITLE-ABS-KEY ({additive manufacturing} AND {solid-state}) (2024). https://www.scopus.com/term/analyzer.uri?sort=plf-f&src=s &sid=84b02a15ae8b3cb7fb535201a054667a &sot=a &sdt=a &sl=57 &s=TITLE-ABS-KEY%28%7badditive+manufacturing%7d+AND+%7bsolid-state%7d%29 &origin=resultslist &count=10 &analyzeResults=Analyze+results Accessed 07.11.2024
2. Brennan MC, Keist JS, Palmer TA (2021) Defects in Metal Additive Manufacturing Processes. Journal of Materials Engineering and Performance 30(7):4808–4818. https://doi.org/10.1007/s11665-021-05919-6#S
3. DebRoy T, Wei HL, Zuback JS, Mukherjee T, Elmer JW, Milewski JO, Beese AM, Wilson-Heid A, De A, Zhang W (2018) Additive manufacturing of metallic components - Process, structure and properties. Progress Mater Sci 92(5):112–224. https://doi.org/10.1016/j.pmatsci.2017.10.001
4. Tang M, Pistorius PC (2017) Anisotropic Mechanical Behavior of AlSi10Mg Parts Produced by Selective Laser Melting. JOM 69(3):516–522. https://doi.org/10.1007/s11837-016-2230-5
5. Cakmak E, Kirka MM, Watkins TR, Cooper RC, An K, Choo H, Wu W, Dehoff RR, Babu SS (2016) Microstructural and micromechanical characterization of IN718 theta shaped specimens built with electron beam melting. Acta Materialia 108:161–175 https://doi.org/10.1016/j.actamat.2016.02.005
6. Huang J, Fu Y, Zhai W, Li R, Zhao X, Lin H, Zhang H, Wang G (2024) Hybrid interlayer hot rolling and wire arc additive manufacturing of Al-Mg alloy: Microstructure, mechanical properties and strengthening mechanism. Journal of Materials Research and Technology 30:7037–7050 https://doi.org/10.1016/j.jmrt.2024.05.085
7. Wei J, He C, Dong R, Tian N, Qin G (2024) Enhancing mechanical properties and defects elimination in 2024 aluminum alloy through interlayer friction stir processing in wire arc additive manufacturing. Mater Sci Eng 901(4):146582. https://doi.org/10.1016/j.msea.2024.146582
8. Xiao Y, Li Y, Shi L, Wu C, Liu H, Sun Z (2023) Experimental and numerical analysis of friction stir additive manufacturing of 2024 aluminium alloy. Materials Today Communications 35:105639 https://doi.org/10.1016/j.mtcomm.2023.105639
9. Bor T, Leede Md, Deunk F, Lind J, Lievestro W, Smit H-J, Ariës R, Dolas V, Helthuis N, Luckabauer M, Akkerman R (2023) Friction screw extrusion additive manufacturing of an Al-Mg-Si alloy. Additive Manufacturing 72(5):103621 https://doi.org/10.1016/j.addma.2023.103621
10. Haridas RS, Gumaste A, Varshney P, Manu BR, Kandasamy K, Kumar N, Mishra RS (2023) SolidStir additive manufacturing: a novel deformation-based additive manufacturing using friction stir technology. JOM 75(10):4231–4241. https://doi.org/10.1007/s11837-023-06063-3
11. Yu HZ, Mishra RS (2021) Additive friction stir deposition: a deformation processing route to metal additive manufacturing. Materials Research Letters 9(2):71–83 https://doi.org/10.1080/21663831.2020.1847211
12. Dilip JJS, Babu S, Rajan SV, Rafi KH, Ram GJ, Stucker BE (2013) Use of Friction Surfacing for Additive Manufacturing. Materials and Manufacturing Processes 28(2):189–194 https://doi.org/10.1080/10426914.2012.677912
13. Rutherford BA, Avery DZ, Phillips BJ, Rao HM, Doherty KJ, Allison PG, Brewer LN, Jordon JB (2020) Effect of thermomechanical processing on fatigue behavior in solid-state additive manufacturing of Al–Mg–Si alloy. Metals 10(7):947. https://doi.org/10.3390/met10070947
14. Rath L, Kallien Z, Roos A, Santos JFd, Klusemann B (2023) Anisotropy and mechanical properties of dissimilar Al additive manufactured structures generated by multi-layer friction surfacing. The International Journal of Advanced Manufacturing Technology 125(5-6):2091–2102 https://doi.org/10.1007/s00170-022-10685-3
15. Phillips BJ, Williamson CJ, Kinser RP, Jordon JB, Doherty KJ, Allison PG (2021) Microstructural and Mechanical Characterization of Additive Friction Stir-Deposition of Aluminum Alloy 5083 Effect of Lubrication on Material Anisotropy. Materials (Basel, Switzerland) 14(21) https://doi.org/10.3390/ma14216732
16. Feng X, Zhang M, Jiang T, Xie Y, Sun Z, Li W (2024) Additive friction stir deposition of an Al–Cu–Mg alloy: microstructure evolution and mechanical properties. Mater Characterization 218(1):114562. https://doi.org/10.1016/j.matchar.2024.114562
17. Qiao Q, Zhou M, Gong X, Jiang S, Lin Y, Wang H, Lam WI, Qian H, Guo D, Zhang D, Kwok CT, Li X, Tam LM (2024) In-situ monitoring of additive friction stir deposition of AA6061: effect of layer thickness on the microstructure and mechanical properties. Additive Manuf 84(11):104141. https://doi.org/10.1016/j.addma.2024.104141
18. Shen Z, Zhang M, Li D, Liu X, Chen S, Hou W, Ding Y, Sun Z, Su Y, Li W, Tian Y (2023) Microstructural characterization and mechanical properties of AlMg alloy fabricated by additive friction stir deposition. Int J Adv Manuf Technol 125(5–6):2733–2741. https://doi.org/10.1007/s00170-023-10952-x
19. Kumar Rajak D, Pagar DD, Menezes PL, Eyvazian A (2020) Friction-based welding processes: friction welding and friction stir welding. J Adhesion Sci Technol 34(24):2613–2637 https://doi.org/10.1080/01694243.2020.1780716
20. Okamura H, Aota K, Sakamoto M, Ezumi M, Ikeuchi K (2002) Behaviour of oxides during friction stir welding of aluminium alloy and their effect on its mechanical properties. Welding Int 16(4):266–275. https://doi.org/10.1080/09507110209549530
21. Ren SR, Ma ZY, Chen LQ (2008) Effect of initial butt surface on tensile properties and fracture behavior of friction stir welded Al-Zn-Mg-Cu alloy. Mater Sci Eng 479(1–2):293–299. https://doi.org/10.1016/j.msea.2007.06.047
22. Phillips BJ, Mason CJT, Beck SC, Avery DZ, Doherty KJ, Allison PG, Jordon JB (2021) Effect of parallel deposition path and interface material flow on resulting microstructure and tensile behavior of Al-Mg-Si alloy fabricated by additive friction stir deposition. Journal of Materials Processing Technology 295:117169 https://doi.org/10.1016/j.jmatprotec.2021.117169
23. Gandra J, Miranda RM, Vilaça P (2012) Performance analysis of friction surfacing. J Mater Process Technol 212(8):1676–1686. https://doi.org/10.1016/j.jmatprotec.2012.03.013
24. Agiwal H, Sridharan K, Pfefferkorn FE, Yeom H (2022) Microstructure and corrosion behavior of friction-surfaced 304L austenitic stainless steels. Int J Adv Manuf Technol 122(3–4):1641–1649. https://doi.org/10.1007/s00170-022-09982-8
25. George Sahaya Nixon R, Mohanty BS, Sathish R (2018) Friction surfacing of AISI 316 over mild steel: A characteriation study. Defence Technology 14(4):306–312 https://doi.org/10.1016/j.dt.2018.03.003
26. Vale N, Fitseva V, Urtiga Filho SL, dos Santos JF, Hanke S (2019) Comparison of friction surfacing process and coating characteristics of Ti-6Al-4V and Ti Grade 1. JOM 71(12):4339–4348. https://doi.org/10.1007/s11837-019-03677-4

27. Dovzhenko G, Hanke S, Staron P, Maawad E, Schreyer A, Horstmann M (2018) Residual stresses and fatigue crack growth in friction surfacing coated Ti-6Al-4V sheets. J Mater Process Technol 262(9):104–110. https://doi.org/10.1016/j.jmatprotec.2018.06.029
28. Gandra J, Pereira D, Miranda RM, Silva RJC, Vilaça P (2013) Deposition of AA6082-T6 over AA2024-T3 by friction surfacing - Mechanical and wear characterization. Surface and Coatings Technology 223:32–40 https://doi.org/10.1016/j.surfcoat.2013.02.023
29. Rao KP, Sankar A, Rafi HK, Ram GDJ, Reddy GM (2013) Friction surfacing on nonferrous substrates: a feasibility study. Int J Adv Manuf Technol 65(5–8):755–762. https://doi.org/10.1007/s00170-012-4214-0
30. Badheka K, Badheka V (2017) Friction surfacing of aluminium on steel: an experimental approach. Mater Today 4(9):9937–9941. https://doi.org/10.1016/j.matpr.2017.06.297
31. Gandra J, Pereira D, Miranda RM, Vilaça P (2013) Influence of Process Parameters in the Friction Surfacing of AA 6082-T6 over AA 2024-T3. Procedia CIRP 7:341–346 https://doi.org/10.1016/j.procir.2013.05.058
32. Dilip JJS, Ram GDJ (2013) Microstructure evolution in aluminum alloy AA 2014 during multi-layer friction deposition. Materials Characterization 86:146–151https://doi.org/10.1016/j.matchar.2013.10.009
33. Rahmati Z, Aval HJ, Nourouzi S, Jamaati R (2021) Effect of friction surfacing parameters on microstructure and mechanical properties of solid-solutionized AA2024 aluminium alloy cladded on AA1050. Materials Chemistry and Physics 269:124756 https://doi.org/10.1016/j.matchemphys.2021.124756
34. Yu M, Zhao H, Zhang Z, Zhou L, Song X, Ma N (2021) Texture evolution and corrosion behavior of the AA6061 coating deposited by friction surfacing. J Mater Process Technol 291:117005 https://doi.org/10.1016/j.jmatprotec.2020.117005
35. Hoffmann M, Roos A, Klusemann B (2024) Investigation of microstructural and mechanical properties in AA2024-T351 multi-layer friction surfacing. Surface Coatings Technol 480(4):130610. https://doi.org/10.1016/j.surfcoat.2024.130610
36. Hammersley AP (2016) FIT2D:a multi-purpose data reduction, analysis and visualization program. J Appl Crystallography 49(2):646–652. https://doi.org/10.1107/S1600576716000455
37. Kallien Z, Hoffmann M, Roos A, Klusemann B (2023) Correlation of Microstructure and Local Mechanical Properties Along Build Direction for Multi-layer Friction Surfacing of Aluminum Alloys. JOM 75(10):4212–4222. https://doi.org/10.1007/s11837-023-06046-4
38. Gollapudi S, Rai N, Kushwaha R, Sabat RK (2021) Crystallographic texture influences on the thermal stability of nanocrystalline materials. J Mater Sci 56(18):11154–11163. https://doi.org/10.1007/s10853-021-05983-2
39. Haessner F (1963) The conditions for the occurrence of the copper-and brass-type texture in rolled face-centered cubic metals. Z Metallkd 54:79–85
40. Hoffmann M, Kallien Z, Antunes Duda E, Klusemann B (2024) Insight into layer formation during friction surfacing: Relationship between deposition behavior and microstructure. Mater Today Commun 41(2):110337. https://doi.org/10.1016/j.mtcomm.2024.110337
41. Hashmi MSJ (ed.): Comprehensive Materials Processing: 13 Volume Set. Elsevier, Amsterdam, Netherlands and Oxford, England and Waltham, Massachusetts (2014). https://ebookcentral.proquest.com/lib/kxp/detail.action?docID=1673593
42. Ehrich, J., Staron, P., Karkar, A., Roos, A., Hanke, S.: Precipitation Evolution in the Heat–Affected Zone and Coating Material of AA2024 Processed by Friction Surfacing. Advanced Engineering Materials 10, 2201019 (2022) https://doi.org/10.1002/adem.202201019
43. Teja PJ, Jain R (2024) Investigating the friction stir additively manufactured AA2024 build and the influence of material flow in enhancing the inter-surface bonding. J Mater Process Technol 333(8):118611. https://doi.org/10.1016/j.jmatprotec.2024.118611
44. Sharifi A, Khodabakhshi F, Gerlich AP (2024) Suppressing anisotropy in additive manufacturing by shear crystallographic texture development during multi-layer friction stir deposition. Mater Sci Eng 903(1):146640. https://doi.org/10.1016/j.msea.2024.146640
45. Zhao Q, Qu Y, Liu Z, Ke H, Jiang S, Wang X, Duan C, Zhai Z, Abdel Wahab M (2024) Texture formation under control of S phase characteristic and tensile property of hot-rolling 2A12 aluminum alloy improved by Brass texture. Mater Sci Eng 899(841):146445. https://doi.org/10.1016/j.msea.2024.146445
46. Hansen N (2004) Hall-Petch relation and boundary strengthening. Scripta Materialia 51(8):801–806. https://doi.org/10.1016/j.scriptamat.2004.06.002
47. Cho KK, Chung YH, Lee CW, Kwun SI, Shin MC (1999) Effects of grain shape and texture on the yield strength anisotropy of Al-Li alloy sheet. Scripta Materialia 40(6):651–657. https://doi.org/10.1016/S1359-6462(98)00481-3
48. Prudhomme, M., Billy, F., Alexis, J., Benoit, G., Hamon, F., Larignon, C., Odemer, G., Blanc, C., Hénaff, G.: Effect of actual and accelerated ageing on microstructure evolution and mechanical properties of a 2024-T351 aluminium alloy. International Journal of Fatigue 107, 60–71 (2018) https://doi.org/10.1016/j.ijfatigue.2017.10.015
49. Cavaliere P, Cerri E, Squillace A (2005) Mechanical response of 2024–7075 aluminium alloys joined by Friction Stir Welding. J Mater Sci 40(14):3669–3676. https://doi.org/10.1007/s10853-005-0474-5
50. Genevois C, Deschamps A, Denquin A, Doisneaucottignies B (2005) Quantitative investigation of precipitation and mechanical behaviour for AA2024 friction stir welds. Acta Materialia 53(8):2447–2458. https://doi.org/10.1016/j.actamat.2005.02.007
51. Ehrich, J., Roos, A., Klusemann, B., Hanke, S.: Influence of Mg content in Al alloys on processing characteristics and dynamically recrystallized microstructure of friction surfacing deposits. Materials Science and Engineering: A 819, 141407 (2021) https://doi.org/10.1016/j.msea.2021.141407
52. Miller, B.A., Shipley, R.J., Parrington, R.J. (eds.): Failure Analysis and Prevention. ASM handbook / prepared under the direction of the ASM International Handbook Committee, vol. volume 11. ASM International, Materials Park, Ohio (2021)
53. MatWeb Material Property Data: Aluminum 2024-T4; 2024-T351. https://www.matweb.com/search/datasheet_print.aspx?matguid=67d8cd7c00a04ba29b618484f7ff7524 Accessed 23.07.2024